Pore Network Extraction for Fractured Porous Media

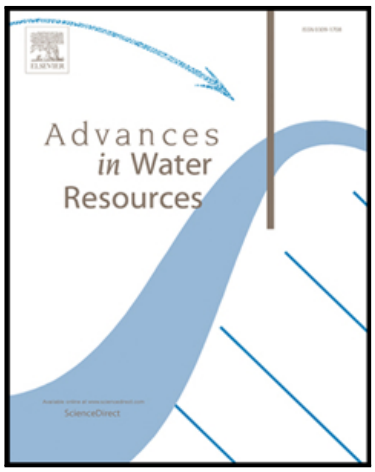

Pore Network Extraction for Fractured Porous Media

Z. Jiang , M.I.J. van Dijke , S. Geiger , J. Ma , G.D. Couples , X. Li

PII: S0309-1708(17)30489-X
DOI: 10.1016/j.advwatres.2017.06.025
Reference: ADWR 2885

To appear in: *Advances in Water Resources*

Received date: 8 May 2017
Revised date: 27 June 2017
Accepted date: 28 June 2017

Please cite this article as: Z. Jiang , M.I.J. van Dijke , S. Geiger , J. Ma , G.D. Couples , X. Li , Pore Network Extraction for Fractured Porous Media, *Advances in Water Resources* (2017), doi: 10.1016/j.advwatres.2017.06.025

Highlights

- Development of a pore-network extraction method for rocks with intersecting fractures embedded in a porous matrix
- Implementation of an efficient shrinking algorithm for simultaneous extraction of medial axes and medial surfaces for arbitrary complex geometries
- Conversion of the skeleton of axes and surfaces into an integrated pore-network model suitable for single- and two-phase flow simulation in fractured rocks

Pore Network Extraction for Fractured Porous Media

Z. Jiang[*, a,b], M.I.J. van Dijke[a], S. Geiger[a], J. Ma[a], G.D. Couples[a], X. Li[b]

[a] Institute of Petroleum Engineering, Heriot-Watt University, Edinburgh, UK

[b] School of Mathematical Sciences, University of Electronic Science and Technology of China, Chengdu, China

*Corresponding author (ZJ6@hw.ac.uk or Zeyun.Jiang@hw.ac.uk)

Abstract

Although flow through fractured rocks involves many different length-scales, it is crucial for the prediction of continuum-scale single- and multi-phase flow functions to understand, at the pore-scale, the interaction between the rock matrix and fractures. Here we present a pore-network extraction method in which the pore diameters and fracture apertures are of similar size. The method involves a shrinking algorithm to extract a hybrid skeleton of medial axes and surfaces, and it includes a workflow to convert the medial surfaces of fractures into dense networks of virtual medial axes, allowing generation of an integrated pore-network for the entire pore space. Appropriate single- and two-phase flow properties are assigned to network elements representing the fractures. We validate the method via comparisons between pore network flow simulations and an analytical solution, direct flow simulations and experimental observations. The network calculations are several orders of magnitude faster than the direct simulations.

Key words: Fracture; Aperture; Medial surface; Pore-network

1 Introduction

Natural fractures are a common feature in rock masses. They can play a major role in fluid flow, thus affecting heat and mass transfer through the bulk mass, with particular effects associated with local transfers between the rock matrix and the fractures (e.g. Berkowitz 2002; Geiger and Emmanuel, 2010; Spence et al., 2014). In many applications, there is a need to understand how multiple, immiscible fluid phases are exchanged between fractures and the matrix pore system (e.g. Schmid and Geiger, 2012), in order to derive relative permeability functions or trapping models at macroscopic scales. Fig. 1(a) shows a fractured limestone core sample that illustrates a heterogeneous rock matrix that is disrupted by a fracture, whose movement has led to non-uniform amounts of opening (aperture) along the fracture. This example demonstrates some key characteristics: a fracture often possesses a complicated

morphology, e.g. variable apertures, non-planarity, and being partly closed. Fractures will typically form a complex network, with other fractures at the same or at different length-scales (Bonnet et al., 2001). It is reasonable to suppose that the fracture segments created during hydraulic fracturing operations will have similar features and relationships. Because of the many interactions that are possible (Couples, 2014; Ebrahimi et al., 2014), both natural and induced fractures may exhibit intricate geometrical and topological relationships between their void space and the adjacent matrix pore system. This paper focuses on the pore-scale of the matrix-fracture interactions, and it introduces models of this particular pore space that enable simulations of fluid exchange between the matrix and adjacent fractures.

Advances in imaging technology make it possible to obtain 3D images of fractured rock samples, for example by using X-ray computed tomography (CT) (e.g., Flannery et al., 1987; Wildenschild and Sheppard, 2012; Karpyn, et al., 2007), as illustrated in Fig. 1(b). It is also possible to acquire high resolution 2D images, such as by optical microscopy, or via the scanning electron microscopes (SEM) (e.g., Lemmens at al., 2010). A simplification that can be useful (and one that is employed here) is to express the model of the sample as a binary image which depicts only the separation of solids and pores (see Fig. 1(c)), and to use this image to characterise the geometry and topology of the fracture void and matrix pore space.

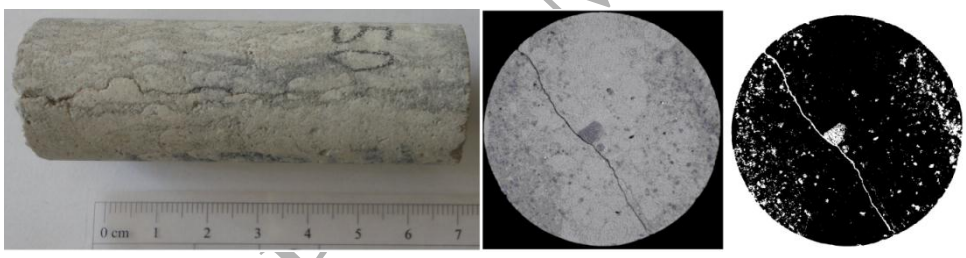

(a) (b) (c)

Fig. 1. A fracture-matrix system in a limestone core: (a) a picture of the core sample with a natural fracture penetrating most of the sample; (b) an X-ray CT section image (in grey scale) perpendicular to the fracture; (c) its segmented binary image (pores and fractures in white and solid in black).

Based on a 3D binary image of a porous medium, its flow properties can be calculated from numerical solutions of the Navier-Stokes equations, combined with evolution equations for the interfaces between multiple fluid phases, directly on the discretised pore space. Examples of such direct approaches include finite element and finite volume methods (e.g. Zaretskiy et al., 2010; Armanini et al., 2014) and Lattice Boltzmann methods (e.g. Shan and Chen, 1993;

Ma et al., 2010), as well as volume of fluid methods (e.g. López et al., 2010; Raeini et al., 2012) and level-set methods (e.g. Prodanovic´ and Bryant, 2006) for multi-phase flow. A key limiting factor of these direct methods is that they are computationally expensive, and that cost increases when multiple fluid phases are considered (Blunt et al., 2013; Friedrich, 1989).

An alternative approach is to simulate fluid flow in a pore-network, which is a reduced-dimension representation of the pore space, and, in its simplest form, consists of an interconnected set of pore nodes and bonds. Initial pore-networks were developed as regular lattices (Fatt, 1965), but current pore-networks are capable of capturing much of the known pore space topology and geometry (Jiang et al., 2007; 2013). Because fluid movement and fluid-phase configurations in each of the pore-network elements can be efficiently determined analytically, subject to local and global constraints on mass and momentum conservation, pore-network flow modelling is computationally much more efficient than the direct simulation approaches. Pore-network methods are naturally well-suited to simulate capillary-dominated multi-phase flow and have been applied successfully to calculate effective flow properties of a wide range of porous media (Vogel and Roth, 2001; Valvatne and Blunt, 2004; Øren and Bakke, 2003; Ryazanov et al., 2009; Jiang et al., 2013). Pore-network flow modelling has also been extended to flow processes where viscous forces are not negligible, although the efficiency of these so-called dynamic network models is significantly reduced compared to the capillary-dominated models (e.g. Yiotsis et al., 2001; Joekar-Niasar and Hassanizadeh, 2012; Blunt, 2017).

The key to the success of pore-network modelling is to extract a network that strictly preserves the pore connectivity expressed in the pore space images and assigns to each (network) element a set of geometric properties (e.g. size and shape) that closely match the values measured directly from the images. The assigned geometrical properties are used to calculate flow characteristics such as conductance and capillary entry pressure. Several methods have been developed for extraction of pore networks from 3D binary images. The maximum ball method identifies the locally widest parts of the pore space as nodes and the remainder as bonds (Silin and Patzek 2006; Dong and Blunt, 2009). A different class of extraction methods identifies the Medial Axis (MA) or skeleton of the pore space and identifies junctions of the MA as nodes (e.g. Lindquist et al., 1996; Øren et al., 1998; Lindquist and Venkatarangan, 1999; Jiang et al., 2007). However, the complex reality of the pore space means that there is no unique way of extracting a pore network and different

extraction methods may lead to significantly different flow properties (Bondino and Kallel, 2013).

According to Leymarie and Levine (1992), the skeleton of an object (here, the object is the pore space) can be determined by the grassfire transformation. In 2D this can be explained by a simple analogy: set fire simultaneously to the entire object boundary (pore walls) and assume that the resulting fire fronts advance into the object at a uniform rate in all directions. The locations where the fire fronts meet form a set of (curved) line segments and/or planes that define the skeleton of the object. The connectivity of the skeleton is the same as that of the original object and the skeleton is located in the centre of the object. In 3D the method leads to the identification of a set of both lines and planes that together define the skeleton. The set of lines is the MA, and the set of planes is called the medial surface (MS). Although the grassfire idea sounds very simple, its implementation in the discrete space (i.e. voxellated images) has proved to be challenging (e.g. Bertrand, 1995; Pudney, 1998; Palágyi, 2002; Telea and Jalba, 2012).

In our previous network generation method (Jiang et al., 2007), we developed a technique that transforms the pore space into an MA (see Fig. 2(a)). This technique is based on an improved distance-ordered shrinking (often called thinning) algorithm (Pudney, 1998) that makes use of the Euclidean distances map of the pore space. The algorithm extracts the MA from any 3D object by sequentially removing so-called simple voxels (Bertrand and Malandain, 1992). The resulting MA is indeed located in the centre of the pore space, preserves the pore space topology and has single-voxel thickness. Subsequently, the MA is then separated into node backbones, which are contained within the maximum inscribed balls centred at axis junctions, and bond backbones (see Fig. 2(b)). Then, the entire pore space is partitioned into nodes and bonds by the (geodesic) distance transformation (see Fig. 2(c)). Additionally, the geometrical properties associated with the nodes and bonds are determined for the use in flow simulations.

(a) (b) (c)

Fig. 2. Visualisation of the pore network extraction workflow of Jiang et al. (2007): (a) extracted MA (blue line) for the pore space (pink); (b) embedded maximum inscribed balls, centred at axis junctions (yellow) as well as at all remaining MA voxels (brown), delineating the node and bond backbones respectively; (c) pore space partitioned as actual nodes (grey) and bonds (light blue).

However, this kind of algorithms also reduces platy objects such as fractures, or other voids with high aspect ratios, into lines, which significantly influences the resulting flow properties. For a proper representation of fractures, it is necessary to extract the MS explicitly (Lee et al., 1994). In digital topology a MS is defined as a set of so-called surface voxels that are characterised locally by topological numbers (Kong et al., 1992; Bertrand, 1995). This definition ensures that the extracted surface is topologically correct, but it gives no indication of how to actually extract the MS. Existing MS extraction methods, such as template-based (e.g. Lee et al., 1994; Bertrand, 1995) and the MLSEC-ST (López et al., 2000) algorithms are more suitable for regular geometries, such as (ideal) fractures with smooth parallel walls. CAD (computer-aided design) models (Lee et al., 1994), and MAT (medial axis transform)-based algorithms (Chatzis and Pitas, 2000; Amenta et al., 2001; Kosinka and Juttler, 2007) lack the ability to extract a MS that preserve the complex geometry of the pore space in fractured rocks. If well preserved a MS can be used as a computing domain in solving controlling (e.g. the Navier-Stokes) equations to calculate the single-phase permeability and to simulate two-phase drainage and imbibition processes (Riasi et al., 2016).

Additionally, a classic pore-network only contains 0D and 1D elements, i.e. nodes and bonds respectively, and there is currently a lack of analytical expressions for flow properties of essentially 2D network elements representing fractures. Several researchers have simulated single- and two-phase flow through a single fracture, by replacing the fracture with a dense pore-network, referred to as virtual network (VN) (Pruess and Tsang, 1990; Rossen and Kumar, 1992; Hughes and Blunt, 2001; Piri and Karpyn, 2007; Jiang et al., 2012). In the VN virtual nodes are placed at local maxima of the fracture aperture connected through a dense

system of virtual bonds. Moreover, channel networks have been developed to represent the intersecting fractures in fractured rocks (Ebrahimi et al., 2014). However, there are currently no suitable methods to construct pore networks that represent fractured rocks with intersecting fractures embedded in a porous matrix, in which the fracture openings (i.e. the void space) are of similar size as the pores in the surrounding matrix.

In this paper we present an efficient and robust algorithm to extract pore networks for fractured porous media by extending our previous pore-network extraction technique developed for non-fractured porous media (Jiang et al., 2007) to fractured porous media. In section 2 we describe the development of the extended shrinking algorithm to extract the MA along with the MS. In section 3 we first develop an algorithm to convert each MS into a virtual medial axis. Then we describe how to generate an integrated network for the entire pore space and how to assign flow-controlling geometric properties to network elements representing fractures. In Section 4 we validate the newly developed pore-network extraction method by comparing the results of single-phase pore-network flow simulation results with an analytical solution, direct flow simulations and experimental observations for a variety of fractured rock models.

2 Medial surface extraction

The starting point for MA extraction is a binary image consisting of a 3D cubic grid of voxels that are either pore or solid. MA extraction (Lee et al., 1994) is the transformation of an object (here, the pore space) into one of minimum (single voxel) thickness that preserves connectivity. This transformation is carried out by sequentially removing object voxels, i.e. converting object voxels to non-object ones.

The criterion for removal of object voxels is that they are simple. A voxel is, almost trivially, defined as simple if its removal does not change the topology of the object (e.g. Bertrand and Malandain, 1992). The shrinking operation finishes when no more simple voxels can be removed, and only the MA remains.

During the shrinking operation, exceptions can be made to retain voxels for specific applications. In our previous work, object voxels were retained that connected the MA to the inlet and outlet faces of the model domain, to facilitate pore-scale flow simulations (Jiang et al. 2007). For fractured porous media, also surface voxels, defined below, will be identified and retained to form the MS.

To ensure the central location of the MA or MS, object voxels are checked for simplicity in layers of increasing Euclidean distance to the pore walls (Jiang et al. 2007). However, the order in which voxels are checked within a given layer of equal Euclidean distance strongly affects the resulting MS and the number of retained surface voxels (e.g. Lee et al., 1994). In the following sections, additional rules will be introduced that reduce the dependence on the checking order and maximise the number of retained surface voxels.

2.1 Surface voxels

A voxel is a surface voxel (see Kong et al., 1992) if its removal leads to the generation of a tunnel (a hole in 2D) through a connected set of object voxels (i.e. the pore space). Following topological convention (Kong et al., 1992) we assume throughout the paper that object voxels have so-called 26-connectivity in 3D, i.e. they are connected if they are face-to-face, edge-to-edge or corner-to-corner adjacent, i.e. 6-, 18- or 26-adjacent respectively. Therefore, a set of connected object voxels is referred to as a 26-component. According to Kong's space partitioning, non-object voxels are assumed to have 6-adjacency, i.e. any two non-object voxels are connected only if they are face-to-face adjacent, and a set of connected non-object voxels is referred to as a 6-component.

The shrinking operation is based on preservation of the topology within the 3x3x3 neighbourhood of any voxel, as this has been proven to preserve the global topology (Kong at al., 1992; Bertrand et al., 1994, 1995). Consequently, a voxel is a surface voxel in the global sense, if it can be identified as a surface voxel in its 3×3×3 neighbourhood, i.e. if its removal leads to the generation of a tunnel in the neighbourhood. In Fig. 3, six neighbourhood configurations are shown that illustrate the surface voxel concept. In the first configuration, removal of the central voxel does not break up the single 26-component, but it does create a tunnel. In other words, converting the central voxel into non-object creates a 6-connection between two non-object 6-components above and below the object component. On the other hand, in the fourth configuration of Fig. 3, no tunnel can be formed, while in the fifth configuration removal of the central voxel breaks up the object 26-component, hence also no tunnel is formed.

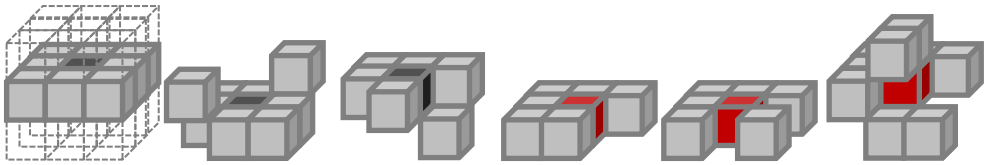

(1, 2) (1, 2) (1, 2) (1, 1) (2, 1) (1, 1)

Fig. 3. Illustration of the concept of surface voxel for six configurations of object voxels within their 3×3×3 neighbourhoods (shown with dotted outlines in the first configuration) centred at the black or red voxels, with the values for T_{26}, T_6 (see text for explanation) given in brackets beneath each configuration. The black voxels are surface voxels but the red ones are not.

Similar to simple voxels, surface voxels can formally be identified in terms of a topological number (Kong et al., 1992). The topological number $T_{26}(p)$ is the number of object 26-components in the 3×3×3 neighbourhood of voxel p (excluding p). $T_6(p)$ is the number of non-object 6-components that consist only of 6- and 18-neighbours of p and that are 6-adjacent to p. Formally, a voxel is simple if

$$T_{26}(p) = T_6(p) = 1, \tag{1}$$

and a voxel is a surface voxel if

$$T_6(p) > 1. \tag{2}$$

In Fig. 3, $T_{26}(p) = 1$ for all configurations except the fifth for which $T_{26}(p) = 2$, while $T_6(p) = 2$ for the first three configurations and $T_6(p) = 1$ for the last three. Observe that in the third configuration the 3×3×3 neighbourhood of the central voxel contains only one non-object 6-component, but there are two components that consist only of 6- and 18-neighbours of p.

As indicated above, the shrinking operation to extract the MS requires sequential removal of all simple object voxels that are not surface voxels, while the latter must be retained. However, simple and surface voxels will not be identified as such until a sufficient number of adjacent voxels within their 3×3×3 neighbourhood have been removed. In particular, surface voxels will only be exposed at the later stages of shrinking, when the remaining object becomes sufficiently (one or two voxels) thin and surrounded by multiple non-object components, as counted by the topological number T_6.

Additionally, the removal of adjacent simple voxels may also prevent identification of a surface voxel. For example, the first configuration in Fig. 3 will turn into the fourth or fifth configuration through the removal of (at least) one 6-adjacent voxel, as this reduces T_6 for the

central voxel. Therefore, if it is not previously identified, the central voxel will not be retained as a surface voxel in subsequent shrinking steps. Similarly, the removal of the bottom 18-adjacent voxel in the third configuration invalidates the surface voxel. On the other hand, the removal of the 26-adjacent voxels in the second configuration does not affect the surface voxel.

Consequently, prior to the removal of a voxel, the T_6 values of its neighbours need to be calculated in order to retain the maximum number of surface voxels. However, this is very time-consuming. To avoid the actual calculation of T_6 in most cases, we introduce the following low-cost pre-checks on 18- and 6-neighbours p of a voxel q.

I. If p is 18-adjacent to q, check whether their shared 6-neighbours are non-object.
II. If p is 6-adjacent to q, check whether two 6-adjacent pairs of their shared 6-neighbours are non-object.

If the results of both pre-checks are negative, a full calculation of $T_6(q)$ is not required, because removal of p will not lead to reconnection of two non-object components, as illustrated in Fig. 4.

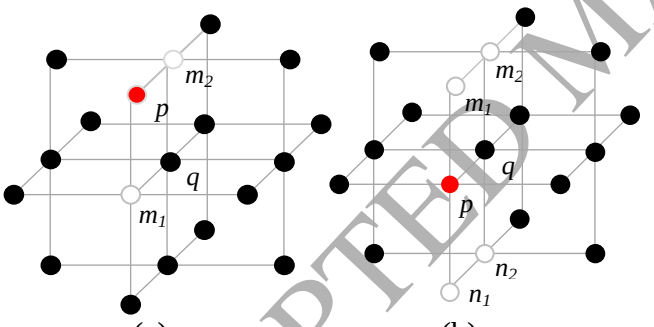

(a) (b)

Fig. 4. Illustration of pre-checks to avoid calculation of $T_6(q)$ before removing simple voxel p. Voxels are represented by vertices, while edges represent the 6-adjacencies within the 18-neighbourhood. Object voxels are coloured black and red, non-object voxels white. (a) The red object voxel p is an 18-neighbour of object voxel q, where removal of p will create a 6-connection between the white non-object voxels m_1 and m_2 (pre-check 1); (b) the red object voxel p is a 6-neighbour of object voxel q, where removal of p will create a 6-connection between the pairs of 6-adjacent non-object voxels $\{m_1, m_2\}$ and $\{n_1, n_2\}$ (pre-check 2).

2.2 Extended shrinking algorithm

By combining the checks for simple and surface voxels with the above pre-checks, we introduce the following extended shrinking algorithm that retains both the MA and the MS. Object voxels are checked for removal in layers of increasing Euclidean distance to non-object voxels (i.e. the pore wall). Within each distance layer voxels are assessed in a raster scan order, and each voxel, p, is checked through the following steps:

1. Check whether p has previously been retained. If so, go to the next voxel.
2. Calculate $T_6(p)$ and check whether p is a surface voxel using Eq. (2). If so, retain p and go to the next voxel.
3. Calculate $T_{26}(p)$ and check whether p is a simple voxel using Eq. (1). If not, retain p and go to the next voxel.
4. For each object 6- and 18-neighbour q of p:
    a. Check whether q has already been retained. If so, go to the next neighbour.
    b. Pre-check whether the removal of p would invalidate q as a surface voxel. If not, go to the next neighbour.
    c. Calculate $T_6(q)$ to check whether q is a surface voxel. If so, retain q.
5. Remove p, and go to the next voxel.

To illustrate how the extended shrinking algorithm works, consider the object voxels in Fig. 5, where all voxels are assumed to be on the same (innermost) distance layer. When voxel 1 is assessed, it is dismissed as a surface voxel in step 2 of the algorithm, but identified as a simple voxel in step 3. To prevent any neighbouring voxels from being invalidated as surface voxels, both object 18-neighbours of voxel 1, voxels 5 and 7, pass the pre-checks in step 4(b), but neither is identified as a surface voxel in step 4(c). Subsequently, voxel 1 is removed (Fig. 5(b)). Voxel 2 is removed similar to voxel 1.

When assessing voxel 3, its remaining 18-neighbour, voxel 9, and 6-neighbour, voxel 4, pass the pre-checks in step 4(b). In step 4(c) voxel 9 is identified and retained as a surface voxel (Fig. 5(c)), whereas voxel 4 is not. Similarly, when assessing voxel 4, voxel 11 is identified as a surface voxel (Fig. 5(d)).

When assessing voxel 5, voxel 8 is identified as a surface voxel and voxel 9 is identified as a previously retained surface voxel in step 4(a). Similarly, when assessing voxel 6, voxels 8 and 9 are identified as previously retained surface voxels. When assessing voxel 7, only voxel 10 is identified as a new surface voxel (Fig. 5(e)).

Subsequently, when voxels 8, 9, 10 and 11 are assessed, they are identified as previously retained surface voxels in step 1. When voxel 12 is assessed, it is itself identified as a surface voxel in step 2, and so is voxel 13. Eventually, a MS of 6 voxels results as shown in Fig. 5(f). It is obvious from Fig. 5 that this is the largest surface that can be extracted from this configuration. Moreover, it follows easily that for this example any checking order will lead to the same retained surface voxels, which is a direct result of pre-checking the neighbours in step 4 of the algorithm.

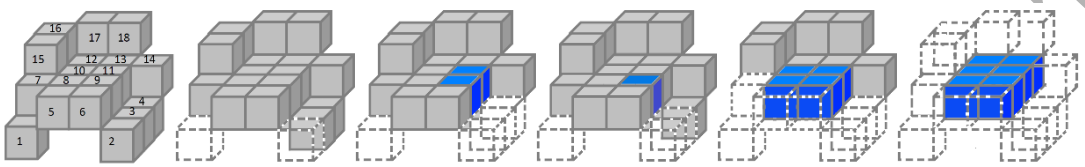

(a) (b) (c) (d) (e) (f)

Fig. 5. Illustration of the extended shrinking algorithm for a structure of 18 grey object voxels. The numbers indicate the order in which the voxels are accessed. Consecutive configurations show the removal of voxels (transparent) and the identification of blue surface voxels.

To highlight the main features of our extended shrinking algorithm, consider the synthetic model of a porous medium shown in Fig. 6(a), in which planar and non-planar "fractures" and "matrix" pore channels intersect. The algorithm produces a hybrid skeleton (Fig. 6(b)), in which the MA is associated with the pore channels and the MS with the fractures. Next, consider the fractured rock model shown in Fig. 6(c), which has been created by superimposing the binary image of a rough and non-planar fracture of variable aperture onto that of a sandstone image. For this model, Fig. 6(d) shows the extracted hybrid skeleton that consists of the MS of the fracture and the MA of the surrounding pore space. These examples demonstrate that the algorithm:

1) automatically distinguishes intersecting, planar and non-planar, fractures and matrix pores, as well as their connections, thus preserving the topology of the void structure in a fractured rock;
2) extracts hybrid skeletons of single-voxel thickness;
3) generates a MS that effectively represent the fractures, in the sense that the fractures can be reproduced from the retained surface voxels and their Euclidean distance values.

Note that the Euclidean distance values for the surface voxels constitute the corresponding fracture aperture maps approximately.

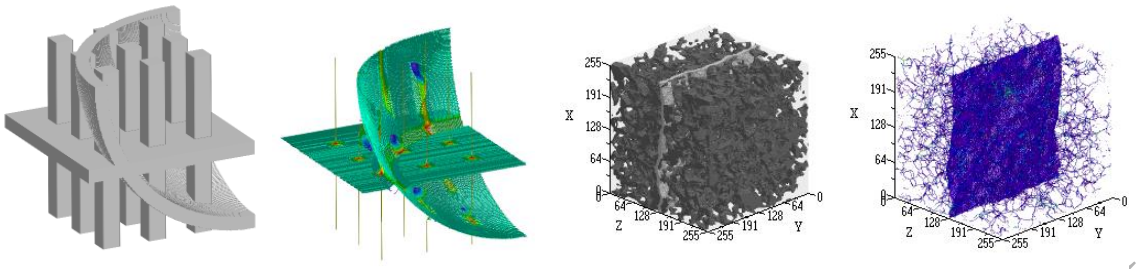

(a) (b) (c) (d)

Fig. 6. (a) Synthetic fracture-matrix space (grey) with (b) its hybrid skeleton, (c) a fractured rock model with (d) its hybrid skeleton. In (b, d) the rainbow colour scheme is used to represent the squared Euclidean distances from the skeleton to the pore walls, ranging from blue (smallest) to red (largest).

3 Network construction

3.1 VMA generation

The next step in creating an integrated network for the entire void space in fractured rocks is conversion of the MS into virtual medial axes (VMA). This conversion is based on the identification of nodes and bonds of virtual networks that approximate the geometry of the underlying fractures. To achieve this, the centres of the virtual nodes will be determined by local maxima of the Euclidean distance values and they will therefore be identified as junctions of the VMA. To ensure that in the resulting network every junction is accessible by fluids from as many directions in the fracture "plane" as possible, the number of branches emerging from each junction should be maximised, resulting in a dense VMA for each fracture. This is achieved through the following three steps, which are illustrated in Fig. 7.

1. Identify surface voxels as junctions of the VMA: Access all surface voxels in decreasing order of Euclidean distance value. If a voxel has not yet been marked, determine its maximum inscribed ball. Only if the ball does not contain any previously marked voxels, mark the voxel as a junction and all other surface voxels within the inscribed ball as being contained (within the ball).
2. Divide all object voxels within the 3×3×3 neighbourhood of each junction voxel into as many different 26-components (branches) as possible: First, check each simple object voxel that is 6-adjacent to the junction voxel and remove it if its removal does not reduce the number of 26-components. Then do the same for every 18-neigbhour.

3. Extract the VMA: Apply the original shrinking algorithm (see Section 1) to all surface voxels that remain after step 2, based on their distance values.

Observe that step 2 changes the topology of the skeleton (see Figs. 7(b, c)). Consistent with this change, shrinking in step 3 creates junctions that connect the branches of the VMA initiated in step 2 (see Fig. 7(d)), in addition to the junction voxels identified in step 1. The shrinking algorithm ensures that the additional junction voxels also correspond to local maxima of the Euclidean distance values. Moreover, shrinking takes into account (retained) voxels of the original MA adjacent to surface voxels, which directly ensures proper connection with the VMA (see Figs. 7(a, d)).

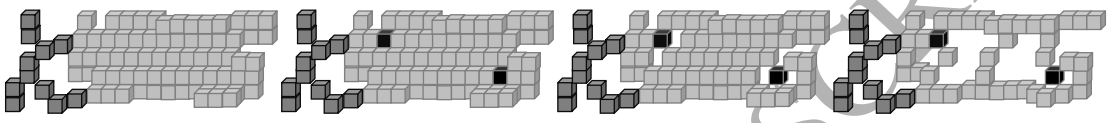

(a) (b) (c) (d)

Fig. 7. Illustration of the three steps in virtual medial axis (VMA) generation. (a) Hybrid skeleton with the MA in dark grey and the MS in light grey; (b) the two (black) voxels in the MS are identified as VMA junctions (step 1); (c) removal of the neighbouring voxels of the junctions (step 2); (d) MS extraction by the original shrinking algorithm (step 3) to generate the VMA consisting of black and grey voxels.

3.2 Hybrid network generation

Following the VMA generation, the entire pore space is represented by a hybrid MA. Subsequently, the original network generation method (see Fig. 2) is used to transform the hybrid MA into a network of nodes and bonds. This network is a hybrid of elements corresponding to: the matrix pore space, the fracture void spaces, and pores that connect fractures and matrix, as illustrated in Fig. 8. Similar to the VMA, we refer to the nodes and bonds representing the fractures as the virtual network (VN).

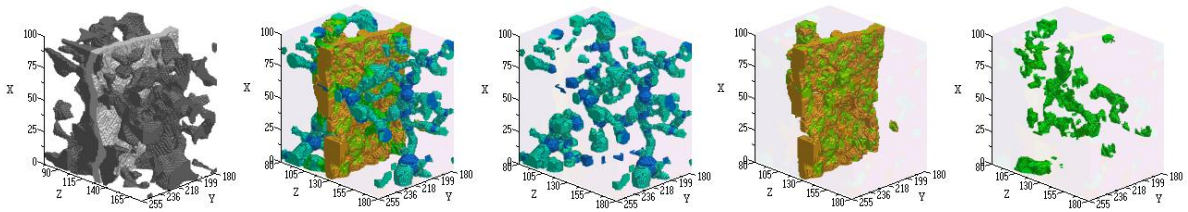

(a) (b) (c) (d) (e)

Fig. 8. (a) A close-up of the fractured rock model shown in Fig. 6(d), (b) the network extracted from it, with network elements for (c) the matrix pore space (nodes in dark blue,

bonds in light blue), (d) the fracture void space (nodes in brown, bonds in green) and (e) the fracture-matrix connections (bonds only in green).

For the matrix and for the fracture-matrix connecting pores, the geometrical properties of the nodes and bonds, such as radius, length and shape factor, are determined as usual (Jiang et al. 2007). For the fractures, the geometrical properties of the nodes and bonds of the VN should be assigned to reflect the underlying fracture apertures, as well as the flow properties, such as hydraulic conductance and drainage capillary entry pressures, that can be expected in fractures.

To determine their flow properties, we assume that the nodes and bonds of the VN are rectangular sections of an ideal fracture with aperture a. Each VN element has a backbone, defined as the corresponding section of the VMA, and a is taken as the average of the apertures for the VMA voxels on the backbone. The width w of each bond is chosen consistent with its actual pore volume V and the path length L of the backbone, i.e. $V=awL$. Because the backbone of a node comprises a number of branches of the VMA, we assume for simplicity that each node is a square section of an ideal fracture with side length w, such that $L=w$ and $V=aw^2$. Consequently, the volumetric flow rate through the rectangular cross-section of a node or bond for a pressure drop ΔP along its length is given by

$$Q = -\frac{wa^3}{12}\,\frac{1}{\mu}\frac{\Delta P}{L} \tag{3}$$

where μ is the dynamic viscosity. In other words, for the VN nodes and bonds the hydraulic conductance g satisfies the cubic law for an ideal fracture (Witherspoon et al., 1980, Zimmerman et al., 1996)

$$g = \frac{wa^3}{12\mu} \tag{4}$$

The capillary entry pressure P_c^e for drainage, e.g. oil displacing water in a water-wet medium, in an ideal fracture is given by the Young-Laplace equation

$$P_c^e = \frac{2\sigma\cos\theta}{a} \tag{5}$$

where σ denotes the interfacial tension and θ denotes the contact angle measured through the wetting phase. Although it represents significant simplification, we assume at present that the capillary entry pressures for VN nodes and bonds are given by equation (5), as this will be

sufficient for the validation presented below. The above adjustments for fracture nodes and bonds have been implemented in our capillary-dominated two-phase flow pore-network simulator (Ryazanov et al. 2009).

4 Validation

To validate the network extraction method, we conduct single-phase and simplified two-phase (drainage) pore-network simulations for single fractures and fractured rocks, and compare these with (1) an analytical solution, based on the cubic law for fracture conductance, (2) finite element flow simulations directly on fractured rock images, (3) Lattice-Boltzmann flow simulations directly on images and (4) experimental observations of fluid occupancies in a rough-walled fracture.

4.1 Analytical solution

In the following we validate our method and implementation by checking the single-phase permeabilities calculated by our network model against the analytical solution for ideal fractures. According to the cubic law, Equation (4), the permeability K_A of a square fracture with aperture a, side length w and cross-sectional area wa can be calculated as $a^2/12$.

A set of 3D models has been generated for square ideal fractures with fixed aperture and varying side lengths. For each fracture model, a VMA has been created and then a VN has been generated as shown in Figs. 9(a, b, c). As can be observed in Fig. 9(c), the positions of the virtual nodes do not entirely align with a square grid as expected, as some randomness occurs in choosing the VMA junction voxels (see Fig. 7(b)) when all apertures are equal. For larger models this finite size effect becomes negligible. For each fracture model, the corresponding permeability K_N is calculated using the network flow simulator, with no-flow conditions on the side boundaries. K_N is plotted against the fracture side length in Fig. 9(d), along with the analytical solution K_A. For sufficiently large side lengths, relative to aperture, K_N converges to K_A, thus validating the virtual network generation. The underestimation for small fracture side lengths is due not only to the finite size effect but also to the fact that the network operates no-flow side boundaries as opposed to the analytical solution (Papanastasiou et al., 1999).

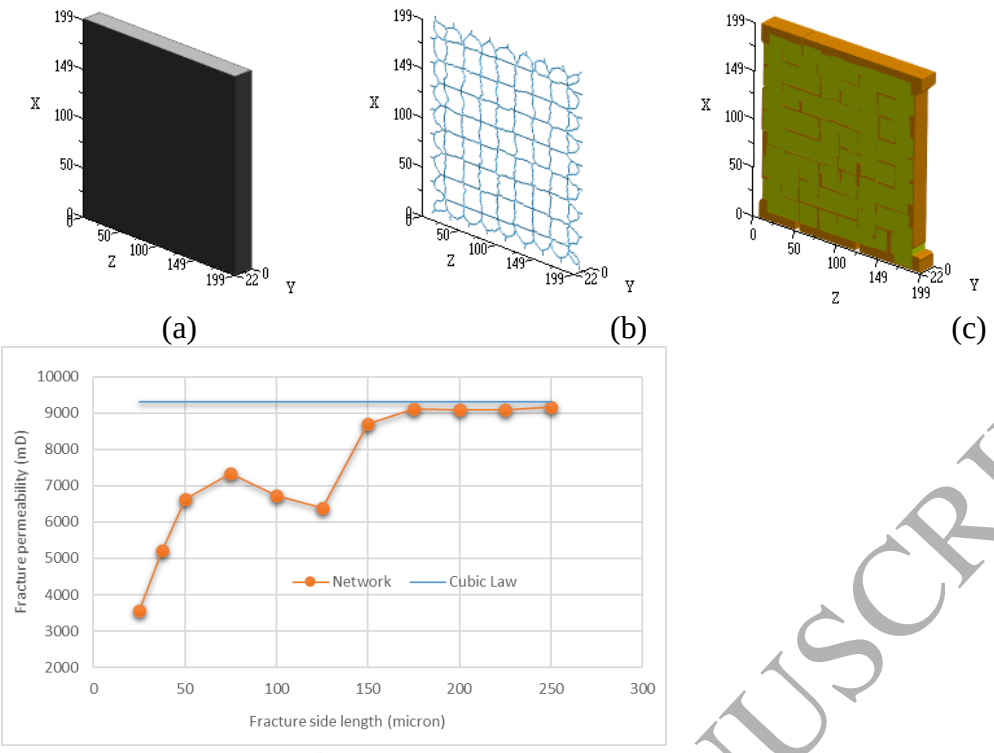

Fig.9. Effect of fracture side length on VN and corresponding permeability: (a) square ideal fracture model (void in grey, wall in black) with aperture of 10.5 μm (21 voxels) and side length of 100 μm (200 voxels); (b) the corresponding VMA; (c) the corresponding VN, in which green cubes represent nodes and bonds are shown in brown (axis labels indicate voxel numbers and flow is simulated in the X-direction); (d) network fracture permeability along with the analytical solution according to the cubic law.

4.2 Direct simulations

In addition to the above validation, we compare permeabilities from our network calculations K_N with those resulting from finite element K_{FE} and Lattice Boltzmann K_{LB} directly on the corresponding pore space images.

First, we consider the binary image of a sandstone rock with 256^3 voxels (voxel size is 5.6μm) on which the image of a natural fracture has been superimposed, similar to Fig. 6(d). The fracture has an average aperture of 34.62 μm and a maximum aperture of 58.2 μm. The fracture has variable but spatially correlated apertures and a few tiny areas have zero aperture. The sandstone sample has an approximately log-normal pore size distribution with diameters ranging from 5.6 μm to 148.82 μm, with an average of 46.19 μm. Consequently, the pore diameters and fracture apertures are of similar size.

Using the methodology described in this paper, networks are extracted for the rock image and the fracture separately, as well as for the fracture-rock combination, which yields a hybrid network. For each model, we calculate K_N and K_{FE} in the X-direction, as shown in Table 1. K_{FE} is calculated from a finite element solution of Stokes equation, using Avizo's Xlab Hydro simulation toolbox (V8.1.1). The deviations for the fracture and the fracture-rock combination are similar to that for the rock, whose network has been extracted using the established original method (Jiang et al. 2007). On a PC (Intel Core i5 CPU, 12G RAM), the computation time for the finite element simulation on the fracture-rock system (27 hours, 42 minutes) is almost 1000 times greater than that for the corresponding combined network extraction and flow simulation (1 minute, 53 seconds).

	Rock	**Fracture**	**Fracture-Rock**
K_N (mD)	1859	1494	3632
K_{FE} (mD)	2038	1380	4108
Deviation (%)	9.6	-7.6	13.1

Table 1: Permeabilities K_N and K_{FE} of the rock, fracture and fracture-rock systems, calculated from pore-network flow and finite volume solutions of Stokes equation, respectively.

Although the flow direction is taken parallel to the fracture, the permeability of the fracture-rock system is larger than the sum of the rock and fracture permeabilities. This indicates that the fracture-matrix connecting pores reflect additional connectivity resulting from the superposition of the two systems.

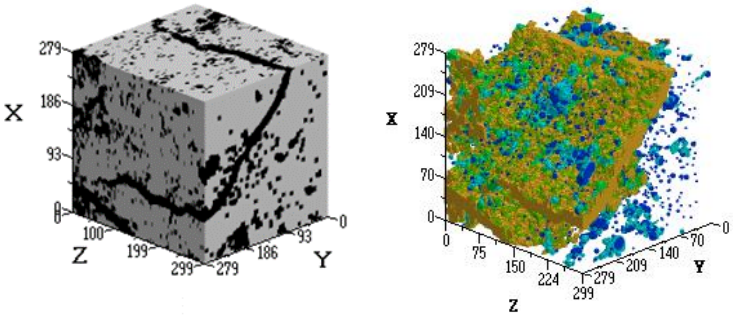

(a) (b)

Fig.10. A 280×280×300 binary image with a voxel resolution of 3.2 μm (a) and the corresponding hybrid network (b) of a naturally fractured rock. Axis labels indicate voxel numbers. Brown represents fracture bonds, yellow fracture nodes, dark blue pore nodes, light blue pore bonds and green fracture-matrix connections.

Second, we consider a binary sub-image derived from a CT scan of a naturally fractured rock, the limestone core sample shown in Fig. 1. Fig. 10 shows the binary sub-image and the corresponding extracted hybrid network. The extraction method clearly reveals several curved, intersecting and (small) parallel fractures. We calculate K_N and K_{LB} in the X- Y- and Z-directions, as shown in Table 2. K_{LB} is calculated using the SHIFT Lattice-Boltzmann code (Ma et al., 2010). Table 2 shows that the K_N and K_{LB} values agree reasonably well.

Flow directions	X	Y	Z
K_N (mD)	2397.61	4963.63	3405.39
K_{LB} (mD)	2304.44	4674.11	3016.53
Deviation (%)	-3.89	-5.83	-11.42

Table 2. Permeabilities K_N and K_{LB} of naturally fractured rock for the image shown in Fig. 10, calculated from our pore-network flow model and our Lattice-Boltzmann model, respectively.

The comparisons above indicate that the generation of the virtual fracture network and the fracture-matrix connecting pores reveals the morphology of fractures, honours the connectivity between fractures and the pore space and preserves the permeability.

4.3 Experimental observations

Karpyn et al. (2007) visualised the aperture distribution and two-phase fluid occupancy in a rough-walled fracture in a Berea sandstone core. Drainage and imbibition experiments were carried out for an oil-water system under ambient conditions. Fluids were injected at slow rates, such that capillary forces dominated. The fracture was strongly water-wet ($\theta = 10^0$) and the mineral oil used had an interfacial tension to water of 41 mN/m. The core was oriented horizontally such that gravitational forces could be neglected. For further experimental details, see Karpyn et al. (2007).

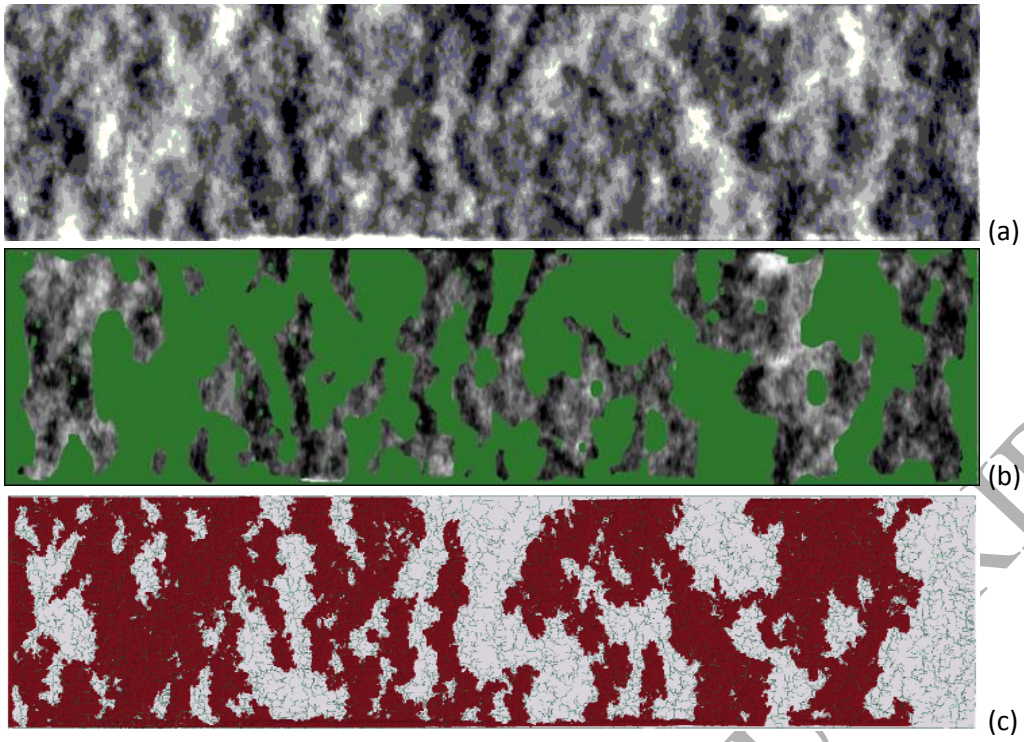

Fig. 11. (a) Fracture aperture map of 860×3116 voxels with 0.033 mm per voxel and apertures varying from zero (black) to maximum (white) of 1.60 mm; (b) oil distributions (green regions) in the experiment (Karpyn et al., 2007) following oil injection from left to right; (c) oil distributions (red area) from the network model. In (c) the lines indicate the VMA generated from the reconstructed fracture.

From the fracture aperture map (see Fig. 11(a)) we reconstructed a 3D fracture model (without matrix connections) that is symmetric about its central plane, similar to the model by Karpyn and Piri (2007). Using our new network extraction method, we obtained a VN for the fracture. We simulated primary drainage in the VN and compared the resulting oil distributions with those visualised by Karpyn et al. (2007) at similar saturations, as shown in Figs. 11(b, c). Note that in both the experiment and the simulation the figures show a view of the 3D fluid distributions projected onto a plane sensibly parallel to the fracture.

Overall, the two oil distributions show good agreement, as in both cases oil has invaded the fracture areas with larger apertures, where those are accessible. The areas near the inlet, the outlet, and the top edge (as shown) have large apertures, and in particular the top edge provides connectivity between different interior fracture areas. However, in the experiment, the oil distribution is not everywhere connected, as would be expected during drainage, which suggests some artefacts related to the experimental procedures. This may explain some of the observed discrepancies between the experimental and simulated distributions.

5 Conclusions

In this paper we have presented a pore network extraction method for fractured rocks. The method comprises an efficient shrinking algorithm that can be used directly on binary images of fractured rocks to extract the hybrid skeleton. The skeleton includes the medial axis for the pore space in the rock matrix, and the medial surfaces for the fracture void spaces, as well as their connections. The new shrinking algorithm has two key features. First, it accurately identifies fractures and their aperture maps, in particular in complex porous media, where the pore diameters and apertures are of similar size, and in the cases where fractures intersect. Secondly, it retains the maximum number of voxels for the medial surfaces to honour the original structure of the fractures. Moreover, the extracted surfaces are largely independent of the voxel scanning order in the algorithm.

The method includes a workflow to convert each medial surface into a dense virtual medial axis, while retaining its connections with the medial axis for the matrix pore space. This allows generation of an integrated network of nodes and bonds for the entire porous medium, using our previously developed method for network construction from a medial axis. Single- and two-phase flow properties are assigned to network elements representing the fractures, by assuming that these elements are sections of an ideal fracture.

We have validated the extraction method by comparing pore network flow simulation results with an analytical solution, with direct flow simulations, and with experimental observations, for a variety of fractured rock models. Importantly, our analysis shows that the network fracture permeabilities correctly converge to the values obtained from the analytical solution and agree well with direct simulations, that our pore-network simulations are several orders of magnitude faster than the direct simulations, and that we obtain oil distributions for drainage of a rough-walled fracture that are very similar to those observed experimentally.

We conclude that the presented pore network extraction method for fractured rocks is accurate, efficient and robust. In future we will implement more accurate expressions for fracture conductances and capillary entry pressures for both drainage and imbibition, and present further case studies for complex fractured rocks.

Acknowledgements

This work is financially supported by Petrobras and BG Group (now Shell), as part of a program of projects in ICCR (International Centre for Carbonate Reservoirs), and also by the NSF Grant of China (no. 61572007). Leonardo Borghi is thanked for the sample shown in Figure 1, Celso Peres Fernandes for providing the corresponding CT images used in this work, and Patrick Corbett for discussion.

References

Armanini, A., Larcher, M., Nucci, E., Dumbser, M. Submerged granular channel flows driven by gravity, Adv Water Resour, (2014), 63, 1–10 http://dx.doi.org/10.1016/j.advwatres.2013.10.007.

Amenta, N., Choi, S., Kolluri, R.K. The power crust, unions of balls, and the medial axis transform. Comp. Geom., (2001), 19(2), 127-153 http://dx.doi.org/10.1016/S0925-7721(01)00017-7.

Berkowitz, B. Characterizing flow and transport in fractured geological media: A review. Adv. Water Res., (2002), 25(8-12), 861-884 http://dx.doi.org/10.1016/S0309-1708(02)00042-8.

Bertrand, G. Simple points, topological numbers and geodesic neighbourhoods in cubic grids. Pattern Rec. Lett. (1994), 15, 1003-101 http://dx.doi.org/10.1016/0167-8655(94)90032-9.

Bertrand, G. A parallel thinning algorithm for medial surfaces. Pattern Rec. Lett. (1995), 16, 979-986 http://dx.doi.org/10.1016/0167-8655(95)00034-e.

Bertrand, G. Malandain, G. A new topological classification of points in 3D images. Proc. European Conf. on Computer Vision, (1992), 588, 710-714 http://dx.doi.org/10.1007/3-540-55426-2_78.

Blunt, M.J., Bijeljic, B., Dong, H., Gharbi, O., Iglauer, S., Mostgaghimi, P., Paluszny, A., Pentland, C. Pore-scale imaging and modelling. Adv. Water Res. (2013), 51, 197-216 http://dx.doi.org/10.1016/j.advwatres.2012.03.003.

Blunt, M.J., Multiphase Flow in Permeable Media: A Pore-Scale Perspective, Cambridge University Press, 2017.

Bondino, I., Kallel, W., Relative Permeabilities from Simulation in 3D, Rock Models and Equivalent Pore Networks: Critical Review and Way Forward, Petrophysics, (2013), 54(6), 538-546.

Bonnet, E., Bour, O., Odling, N.E., Davy, P., Scaling of Fracture Systems in Geological Media, Reviews of Geophysics, (2001), 39(3), 347-383 http://dx.doi.org/10.1029/1999RG000074.

Chatzis, V., Pitas, I. Interpolation of 3-D binary images based on morphological skeletonisation. IEEE Trans. on Medical Imaging. (2000), 19(7), 699-710 http://dx.doi.org/10.1016/10.1109/42.875192.

Couples, G.D., Geomechanical impacts on flow in fractured reservoirs, *In*. Spence, G.H., Redfern, J., Aguilera, R., Bevan, T.G., Cosgrove, J.W., Couples, G.D. & Daniel, J.-M. (eds) Advances in the Study of Fractured Reservoirs. Geological Society, London, Special Publications, (2014), 374, http://dx.doi.org/10.1144/SP374.17.

Dong, H., Blunt, M.J. Pore-network extraction from micro-computerized tomography images. Phys. Rev. E, (2009), 80:036307 http://dx.doi.org/10.1103/PhysRevE.80.036307.

Ebrahimi, A.N., Wittel, F.K., Araújo, N.A.M., Herrmann, H.J., Multi-scale approach to invasion percolation of rock fracture networks, J. Hydrol, (2014), 519, 353-363. http://dx.doi.org/ 10.1016/j.jhydrol.2014.07.012.

Fatt, I. The network model of porous media I. Capillary pressure characteristics. Trans AIME, (1956), 207, 144-159.

Flannery, B.P., Deckman, H.W., Roberge, W.G., D'Amico, K.L. Three-dimensional X-ray microtomography. Science, (1987), 237, 1439–1444 http://dx.doi.org/10.1126/science.237.4821.1439.

Friedrich, K. Application of fracture mechanics to composite materials, Elsevier Science Publishers B. V., 1989.

Geiger, S., Emmanuel, S. Non-Fourier thermal transport in fractured geological media. Adv. Water Res. (2010), 46(7), W07504 http://dx.doi.org/10.1029/2009WR008671.

Hughes, R.G., Blunt, M.J., Network modelling of multiphase flow in fractures, Adv, Water Res., (2001), 24, 409-421 http://dx.doi.org/10.1016/S0309-1708(00)00064-6.

Lee, T.C., Kashyap, R.L., Chu, C.N. Building skeleton models via 3-D medial surface/axis thinning algorithms. *CVGIP:* Graph. Model Im. Proc., (1994), 56(6), 462-478 http://dx.doi.org/10.1006/cgip.1994.1042.

Leymarie, F., and Levine, M.D.,Simulating the Grassfire Transform Using an Active Contour Mode, IEEE Transactions on Pattern Analysis and Machine Intelligence, (1992), 14(1), 56-75 http://dx.doi.org/10.1109/34.107013.

Lindquist, W.B., Lee, S.M, Coker, D.A. Jones, K.W., Spanne, P., Medial axis analysis of void structure in three-dimensional tomographic images of porous media, J. Geophys. Res. Solid Earth, 101 (B4) (1996), 8297–8310 http://dx.doi.org/10.1029/95JB03039.

Lindquist, W. B., and Venkatarangan, A. Investigating 3D geometry of porous media from high resolution images, Phys. Chem. Earth, (1999), 25(7), 593 – 599 http://dx.doi.org/10.1016/S1464-1895(99)00085-X.

Lemmens, H.J., Butcher, A.R., Botha, P.W. FIB/SEM and automated mineralogy for core and cuttings analysis. In: Proceedings of the SPE Russian oil and gas conference and exhibition, (2010), 26–28 October, Moscow, Russia, SPE 136327 http://dx.doi.org/10.2118/136327-MS.

López, J., Gómez, P., Hernández, J. A volume of fluid approach for crystal growth simulation. J. Comput. Phys. (2010), 229, 6663–6672 http://dx.doi.org/10.1016/j.jcp.2010.05.026.

López, A.M., Lloret, D., Serrat, J., Villanueva, J. Multilocal creasenses based on the level-set extrinsic curvature. Comput. Vis. Image Underst., (2000), 77, 111-144 http://dx.doi.org/10.1006/cviu.1999.0812.

Joekar-Niasar, V., & Hassanizadeh, S. M. Analysis of fundamentals of two-phase flow in porous media using dynamic pore-network models: A review. Crit. Rev. Environ. Sci. Technol., (2012), 42(18), 1895-1976 http://dx.doi.org/10.1080/10643389.2011.574101.

Jiang, Z., Wu, K., Couples, G.S., van Dijke, M.I.J., Sorbie, K.S., Ma, J. Efficient extraction of networks from three-dimensional porous media. Water Resour. Res., (2007), 43, W12S03 http://dx.doi.org/10.1029/2006WR005780.

Jiang, Z. van Dijke, M.I.J., Geiger, S., Couples, G., Wood, R. Extraction of fractures from 3D rock images and network modelling of multi-phase flow in fracture-pore systems. SCA2012-57, Aberdeen, Scotland, UK, 27-30, 2012.

Jiang, Z., van Dijke, M.I.J., Sorbie, K.S., Couples, G.D. Representation of multi-scale heterogeneity via multi-scale pore networks. Water Resour. Res., (2013), 49(9), 5437-5449 http://dx.doi.org/10.1002/wrcr.20304.

Karpyn, Z.T., Grader, A.S., Halleck, P.M. Visualization of fluid occupancy in a rough fracture using micro-tomography. J. Colloid Interf. Sci., (2007), 307(1), 181-187 http://dx.doi.org/10.1016/j.jcis.2006.10.082.

Kong, T.Y., Roscoe, A.W., Rosenfeld, A., Concepts of digital topology. Topol. Appl., (1992), 46(3), 219-262 http://dx.doi.org/10.1016/0166-8641(92)90016-S.

Kosinka, J., Juttler, B. MOS surface: Medial surface transforms with rational domain boundaries. Mathematics of Surfaces XII, R. Sabin. J. Winkle, LNCS 4647, Springer, (2007), 245-263 http://dx.doi.org/10.1007/978-3-540-73843-5_15.

Ma, J., Wu, K., Jiang Z., Couples, G.D. SHIFT: an implementation for lattice Boltzmann simulation in low-porosity porous media. Phys. Rev. E, (2010), 81(5), 61-76 https://doi.org/10.1103/PhysRevE.81.056702.

Øren, P.E., Bakke, S. Process based reconstruction of sandstones and prediction of transport properties. Transport Porous Med., (2003), 46(2–3), 311–343 http://dx.doi.org/10.1023/A:1015031122338.

Palágyi, K., A 3-subiteration 3D thinning algorithm for extracting medial surfaces. Pattern Rec. Lett., (2002), 23, 663-675 http://dx.doi.org/10.1016/S0167-8655(01)00142-8.

Papanastasiou, T., Georgiou, G., Alexandrou, A.N., Viscous fluid flow, CRC Press, 1999.

Piri, M., Karpyn, Z.T. Prediction of fluid occupancy in fractures using network modelling and x-ray microtomography. I, II. Phys. Rev. E, (2007), 76(5-6), 016316 http://dx.doi.org//10.1103/PhysRevE.76.016315.

Prodanovic´, M., and Bryant, S.L., A level set method for determining critical curvatures for drainage and imbibition, J. Colliod Interface Sci., (2006), 304, 442-448 http://dx.doi.org/10.1016/j.jcis.2006.08.048.

Pruess, K., Tsang, Y.W. On two-phase relative permeability and capillary pressure of rough-walled rock fractures. Water Resour. Res., (1990), 26(19), 1915-1926 http://dx.doi.org/10.1029/WR026i009p01915.

Pudney, C. Distance-ordered homotopic thinning: A skeletonization algorithm for 3D digital images. Comput. Vis. Image Und., (1998), 72(3), 404-413 http://dx.doi.org/10.1023/A:1009829415835.

Raeini, A.Q., Blunt, M.J., Bijeljic, B. Modelling two-phase flow in porous media at the pore scale using the volume-of-fluid method. J. Comput. Phy., (2012), 31(17), 5653-5668 http://dx.doi.org/10.1016/j.jcp.2012.04.011.

Riasi, M.S., Palakurthi, N.K., Montemagno, C., Yeghiazarian, Li. A Feasibility Study of the Pore Topology Method (PTM), A Medial Surface-Based Approach to Multi-phase Flow Simulation in Porous Media, Transp. Porous Med., (2016), 115, 519-539 http://dx.doi.org/10.1007/s11242-016-0720-0.

Rossen, W.R., Kumar, A.T.A. Single- and two-phase flow in natural fractures, Paper SPE 24915, Proc. 67th SPE Annular Technical Conference and Exhibition, Washinton D.C. 1992, http://dx.doi.org/10.2118/24915-MS.

Ryazanov, A.V., van Dijke, M.I.J., Sorbie, K.S. Two-phase pore-network modelling: existence of oil layers during water invasion, Transp. Porous. Med., (2009), 80, 79-99 http://dx.doi.org/10.1007/s11242-009-9345-x.

Schmid, K.S., Geiger, S., Universal scaling of spontaneous imbibition for water-wet systems, Water Resour. Res.,, (2012), 48, W03507 http://dx.doi.org/10.1029/2011WR011566.

Shan,X, Chen, H. Lattice Boltzmann model for simulating flows with multiple phases and components, Phys. Rev. E, (1993), 47, 1815 http://dx.doi.org/10.1103/PhysRevE.47.1815.

Silin, D., and Patzek, T., Pore space morphology analysis using maximal inscribed spheres, Physica A, (2006|), 371, 336 – 360 http://dx.doi.org/10.1016/j.physa2006.04.048.

Spence, G.H., Couples, G.D., Bevan, T.G., Aguilera, R., Cosgrove, J.W., Daniel, J-M., Redfern, J. Advances in the study of naturally fractured hydrocarbon reservoirs: a broad integrated interdisciplinary applied topic. *In*. Spence, G.H., Redfern, J., Aguilera, R., Bevan, T.G., Cosgrove, J.W., Couples, G.D. & Daniel, J.-M. (eds) Advances in the Study of Fractured Reservoirs. Geological Society, London, Special Publications, (2014), 374, 1-22 http://dx.doi.org/10.1144/SP374.19.

Telea, A., Jalba, A.C. Computing Curve skeleton from medial surfaces of 3D shapes, BG UK Theory and Practice of Computer graphics, (2012), 99-106 http://dx.doi.org/10.2312/LocalChapterEvents/TPCG/TPCG12/099-106.

Valvatne P.H., Blunt M.J. Predictive pore-scale modeling of two-phase flow in mixed wet media. Water Resour. Res., (2004), 40(7), W07406: 1-21 http://dx.doi.org/10.1029/2003WR002627.

Vogel, H.J., Roth, K. Quantitative morphology and network representation of soil pore structure. Adv. Water Res., (2001), 24, 233-242 http://dx.doi.org/10.1016/S0309-1708(00)00055-5.

Wildenschild, D., Sheppard A.P. X-ray imaging and analysis techniques for quantifying pore-scale structure and processes in subsurface porous medium systems, Adv. Water Res., (2012), 51, 217-246 http://dx.doi.org/10.1016/j.advwatres.2012.07.018.

Witherspoon, P. Wang, J.S.Y., Iwai, K., J.E. Gale, J.E. Validity of Cubic Law for fluid flow in a deformable rock fracture. Water Resource Res., (1980), 16(6), 1016-1024 http://dx.doi.org/10.1029/WR016i006p01016.

Yiotsis, A.G., Stubos, A.K., Boudouvis, A.G., Yortsos, Y.C. A 2D pore-network model of the drying of single-component liquids in porous media. Adv. Water. Resour., (2001), 24,439-460 http://dx.doi.org/10.1016/S0309-1708(00)00066-X.

Zaretskiy, Y., Geiger, S., Sorbie, K., Forster, M., Efficient flow and transport simulations in reconstructed 3D pore geometries, Adv. Water Res., (2010), 33, 1508-1516 http://dx.doi.org/10.1016/j.advwatres.2010.08.008.

Zimmerman, R. W., and Bodvarsson, G.S. Hydraulic conductivity of rock fractures, Transp. Porous Media, (1996), 23, 1-30 http://dx.doi.org/10.1007/BF00145263.